Deconvolution-based distortion correction of EPI using analytic single-voxel point-spread functions

Franz Patzig | **Toralf Mildner** | **Torsten Schlumm** | **Roland Müller** | **Harald E. Möller** 🆔 🐦

Max Planck Institute for Human Cognitive and Brain Sciences, Leipzig, Germany

Correspondence
Harald E. Möller, Max Planck Institute for Human Cognitive and Brain Sciences, Stephanstraße 1A, 04103 Leipzig, Germany.
Email: moeller@cbs.mpg.de

Purpose: To develop a postprocessing algorithm that corrects geometric distortions due to spatial variations of the static magnetic field amplitude, B_0, and effects from relaxation during signal acquisition in EPI.

Theory and Methods: An analytic, complex point-spread function is deduced for k-space trajectories of EPI variants and applied to corresponding acquisitions in a resolution phantom and in human volunteers at 3 T. With the analytic point-spread function and experimental maps of B_0 (and, optionally, the effective transverse relaxation time, T_2^*) as input, a point-spread function matrix operator is devised for distortion correction by a Thikonov-regularized deconvolution in image space. The point-spread function operator provides additional information for an appropriate correction of the signal intensity distribution. A previous image combination algorithm for acquisitions with opposite phase blip polarities is adapted to the proposed method to recover destructively interfering signal contributions.

Results: Applications of the proposed deconvolution-based distortion correction ("DecoDisCo") algorithm demonstrate excellent distortion corrections and superior performance regarding the recovery of an undistorted intensity distribution in comparison to a multifrequency reconstruction. Examples include full and partial Fourier standard EPI scans as well as double-shot center-out trajectories. Compared with other distortion-correction approaches, DecoDisCo permits additional deblurring to obtain sharper images in cases of significant T_2^* effects.

Conclusion: Robust distortion corrections in EPI acquisitions are feasible with high quality by regularized deconvolution with an analytic point-spread function. The general algorithm, which is publicly released on GitHub, can be straightforwardly adapted for specific EPI variants or other acquisition schemes.

KEYWORDS
deconvolution, echo-planar imaging, geometric distortion, magnetic field inhomogeneity, point-spread function, transverse relaxation

1 | INTRODUCTION

Echo-planar imaging[1] is the most widely used fast MRI technique, especially in functional MRI (fMRI), diffusion-weighted (dw) MRI or studies of tissue perfusion. Such experiments typically use single-shot acquisitions with a relatively long echo train and a concomitantly low effective bandwidth along the phase-encoding (PE) direction. Consequently, the in-plane resolution may be degraded by blurring related to transverse relaxation with an effective rate $R_2^* = 1/T_2^*$ during image acquisition.[2] Even more prominent are geometric distortions due to spatially varying offsets of the Larmor frequency, $\Delta\omega_0 = 2\pi\Delta\nu_0$. Such offsets may result from the presence of compounds of different magnetic susceptibility in the imaged object or from eddy currents induced by switching magnetic field gradients.[2,3] As R_2^* and $\Delta\nu_0$ increase with the amplitude of the static magnetic field, B_0, the related image artifacts become increasingly prominent at higher field. They can be mitigated with parallel imaging techniques.[4,5] However, applications may be limited by the performance of the receive coil, such as in fMRI at laminar resolution, where the FOV may be of the order of the size of the coil elements.[6-8]

A panoply of approaches has been developed to correct distortions in EPI. One family of algorithms involves non-rigid registration of the EPI data to geometrically correct structural scans, which are typically available in parallel to fMRI or dw-MRI acquisitions.[9] A physics-based procedure includes the calculation of a B_0 "field map"[10] from the signal phase in a separate multiple gradient-echo (GE) experiment and permits a quantitative a priori characterization of magnetic field inhomogeneities.[11] With the "conjugate phase method," the EPI k-space data can then be corrected by demodulation of the offset-induced phase error.[12] An accelerated version of the conjugate phase method is the so-called "frequency-segmented approach" (or "multifrequency reconstruction" [MFR]).[13,14] These techniques are capable of correcting geometrical shifts for any k-space trajectory. However, they may lack an adequate intensity correction in areas of large B_0 variations. Alternatively, "k-space energy spectrum analysis" has been proposed for dynamic field mapping and distortion correction directly from the EPI data.[15] "Reversed gradient approaches" use information from two EPI acquisitions with opposite polarity of the phase blips.[16-18] It is then assumed that both acquisitions yield identical signal intensity but geometric distortions in opposite directions, and that they can be corrected to the same undistorted template. A popular algorithm of this class is TOPUP,[19,20] implemented in FSL.[21] Recent simulations suggest that multiple-PE methods, such as TOPUP, are more accurate than multiple-echo (ME) B_0 mapping, while registration-based approaches yielded the poorest corrections.[22]

Point-spread function (PSF) mapping techniques include a preparation scan to obtain a measured PSF_n for each image voxel n.[23-26] They were proposed to outperform field-map techniques if equal time is allowed for PSF_n mapping and field mapping.[24] An extended version includes the combination of two distortion-corrected EPI data sets of opposite blip polarity for additional image correction.[27]

Most of these techniques inherently assume that the subject (and hence, the distortions) remains static during the experiment. This does not capture local B_0 fluctuations due to head motion, respiration, or scanner drifts. Dynamic distortion correction methods may address this limitation in fMRI time series.[15,28-31] They often rely on ME acquisitions or multichannel phase information.

In the current work, we introduce a PSF method for deconvolution-based distortion correction (referred to as "DecoDisCo"). It uses information from a field map obtained from either ME or multiple-PE acquisitions. Unlike previous PSF-based corrections, it relies on prior knowledge of an analytic PSF_n that considers the particular k-space trajectory.[32] From this input, a deconvolution operator is devised for a regularized computation of distortion-corrected and intensity-corrected data. Apart from frequency offsets, effects from T_2^* relaxation are also considered in the mathematical description, for potential deblurring. Furthermore, an algorithm is presented for the combination of images recorded with opposite blip polarity. Results from applications to in vivo imaging of human brain are compared to those obtained with existing methods including MFR and TOPUP.

2 | THEORY

We restrict our consideration to 2D-EPI variants and assume that frequency encoding is performed along the x-axis in N_x steps and PE along the y-axis in N_y steps. Next, we define matrices $\mathbf{A}$ and $\tilde{\mathbf{A}}$ of dimension $N_x \times N_y$ containing complex-valued signal intensities in an idealized undistorted object and in the measured image, respectively. The image is a convolution of a spatially varying complex PSF and the object.[33] For EPI, only distortions in PE direction are relevant, whereas the frequency-encoding bandwidth is typically large enough to keep distortions below the voxel size.[2] Instead of the entire object $\mathbf{A}$ (and image $\tilde{\mathbf{A}}$), it is therefore sufficient to consider an arbitrary object column $\mathbf{a}$ in PE dimension. Each voxel n of this column ($0 \leq n \leq N_y - 1$) is characterized by its specific object intensity a_n and an individual PSF_n, depending on the distribution of Larmor frequencies. The PSF_n is a function of the k-space trajectory, the TE, the local frequency offset $\Delta\nu_{0,n}$, and the local relaxation time $T_{2,n}^*$, whereby the latter two reflect the mean and width of the intravoxel frequency distribution, respectively.[34] Due to the convolution,

PSF_n contributes intensity to any voxel m of the corresponding column $\tilde{\mathbf{a}}$ of image intensities ($0 \leq m \leq N_y - 1$).

2.1 | Analytic point-spread functions

The PSF_n is obtained by an inverse Fourier transform ($\mathcal{F}^{-1}$) of the modulation transfer function of the pulse sequence in k-space. Consideration of $\Delta\nu_{0,n}$ and $T^*_{2,n}$ and a truncated acquisition window leads to the following k-space weighting function for GE-EPI at the location of voxel n[35]:

$$H_{\text{GE},\,n}(t) = e^{-t/T^*_{2,\,n}} \cdot e^{i2\pi\Delta\nu_{0,\,n}t} \cdot \mathbf{1}_{[k_{y,\,min},\,k_{y,\,max}]}(k_y), \quad (1)$$

where t is the sampling time of k-space coordinate k_y (with $t = 0$ defined by the onset of the acquisition window); and ι is the imaginary unit. The k-space lines are separated by increments of $\Delta k_y = 1/FOV_y$ and cover a range from $k^+_{y,min} = -(2f_p-1)N_y\Delta k_y/2$ to $k^+_{y,max} = +N_y\Delta k_y/2$ and from $k^-_{y,min} = -N_y\Delta k_y/2$ to $k^-_{y,max} = (2f_p-1)N_y\Delta k_y/2$ for bottom-up (indicated by "+") and top-down (indicated by "–") trajectories, respectively. The fraction $f_p \in [1/2, 1]$ considers a potential partial Fourier GE (pGE) acquisition in PE direction.[36] Truncation of the acquisition window is accounted for by the indicator function $\mathbf{1}_{[a,b]}(x) \equiv 1$ if $x \in [a,b]$ and 0 elsewhere. With the echo spacing Δt_e and the nominal image resolution $\Delta y = (N_y\Delta k_y)^{-1}$, the sampling time can be rewritten as

$$t^\pm = \left(f_p - \frac{1}{2}\right)N_y \cdot \Delta t_e \pm \Delta y \cdot k_y \cdot N_y \cdot \Delta t_e. \quad (2)$$

Insertion into Equation 1, inverse Fourier transform and consideration of a normalization factor ε yield

$$PSF^\pm_{\text{GE},n}(y) = \varepsilon\mathcal{F}^{-1}\left\{H^\pm_{\text{GE},n}(k_y)\right\} = \frac{1}{\Delta y} \cdot \frac{e^{(2f_p-1)q^{*\pm}_n} - e^{-q^{*\pm}_n}}{2q^{*\pm}_n} \quad (3)$$

with the dimensionless spatial coordinate

$$q^{*\pm}_n(y) = \frac{N_y \cdot \Delta t_e}{2T^*_{2,n}} - i\pi\left(\Delta\nu_{0,n} \cdot N_y \cdot \Delta t_e \pm \frac{y}{\Delta y}\right). \quad (4)$$

For full-Fourier GE (fGE) acquisitions, Equation 3 can be further simplified according to

$$PSF^\pm_{\text{fGE},n}(y) = \frac{1}{\Delta y} \cdot \frac{\sinh\left(q^{*\pm}_n\right)}{q^{*\pm}_n}. \quad (5)$$

Corresponding results for spin-echo (SE) EPI are presented in Appendix A.1.

In partial-Fourier acquisitions, missing samples in one tile of k-space are computed as complex conjugates of the (measured) corresponding lines in the opposite tile ("conjugate filling"), which has not been considered above. The PSF_n is then obtained as the sum of the result from Equation 3 for the acquired tile plus an equivalent expression (with time reversal) for the computed tile, as follows:

$$PSF^\pm_{\text{conjGE},n}(y) = \frac{1}{\Delta y} \cdot \left[\frac{e^{\pm(2f_p-1)q^{*+}_n} - e^{-q^{*+}_n}}{2q^{*+}_n} + \frac{e^{\mp(2f_p-1)q^{*-}_n} - e^{-q^{*-}_n}}{2q^{*-}_n}\right]. \quad (6)$$

An EPI variant referred to as double-shot EPI with center-out trajectories and intrinsic navigation (DEPICTING)[37] acquires two k-space segments in one *TR*. Both trajectories start at the central line and progresses outward in opposite directions by using opposite phase blip polarities. The sampling time of these trajectories can be written as

$$t^{\text{co}} = \Delta y \cdot |k_y| \cdot N_y \cdot \Delta t_e. \quad (7)$$

This leads to a PSF_n that is also obtainable from Equation 6 by assuming pGE-EPI with conjugate filling of one half of k-space ($f_p = 1/2$):

$$PSF_{\text{D},n}(y) = \frac{1}{\Delta y} \cdot \left(\frac{1 - e^{-q^{*+}_n}}{2q^{*+}_n} + \frac{1 - e^{-q^{*-}_n}}{2q^{*-}_n}\right). \quad (8)$$

These derivations of PSF_n can be adapted for other k-space trajectories. Parallel imaging[4,5] with an acceleration factor R is straightforwardly accounted for by rewriting $\Delta k_y \to \Delta k_y \cdot R$, $FOV_y \to FOV_y/R$ and $N_y \to N_y/R$, whereas $\Delta y = FOV_y/N_y$ remains unchanged. The corresponding PSF_n is therefore obtained by replacing N_y by N_y/R in Equations 2, 4, and 7.

## 2.2 | Distortion correction by deconvolution

The image intensity $\tilde{a}_m$ of a voxel m is the sum of all object intensities a_n weighted by the value of PSF_n at a position $y_{mn} = (m-n) \cdot \Delta y$ according to the distance between voxels n and m:

$$\tilde{a}_m = \sum_{n=0}^{N_y-1} PSF_n(y_{mn}) \cdot a_n. \quad (9)$$

A compact expression for an entire image column (along the PE direction) is

$$\tilde{\mathbf{a}} = \mathbf{PSF} \cdot \mathbf{a}, \quad (10)$$

where $\mathbf{PSF}$ is a matrix of size $N_y \times N_y$. Figure 1A shows an experimentally obtained $\Delta\nu_{0,n}$-column. The magnitude of the corresponding $\mathbf{PSF}^+_{\text{fGE}}$ matrix is given in Figure 1B. Nonzero
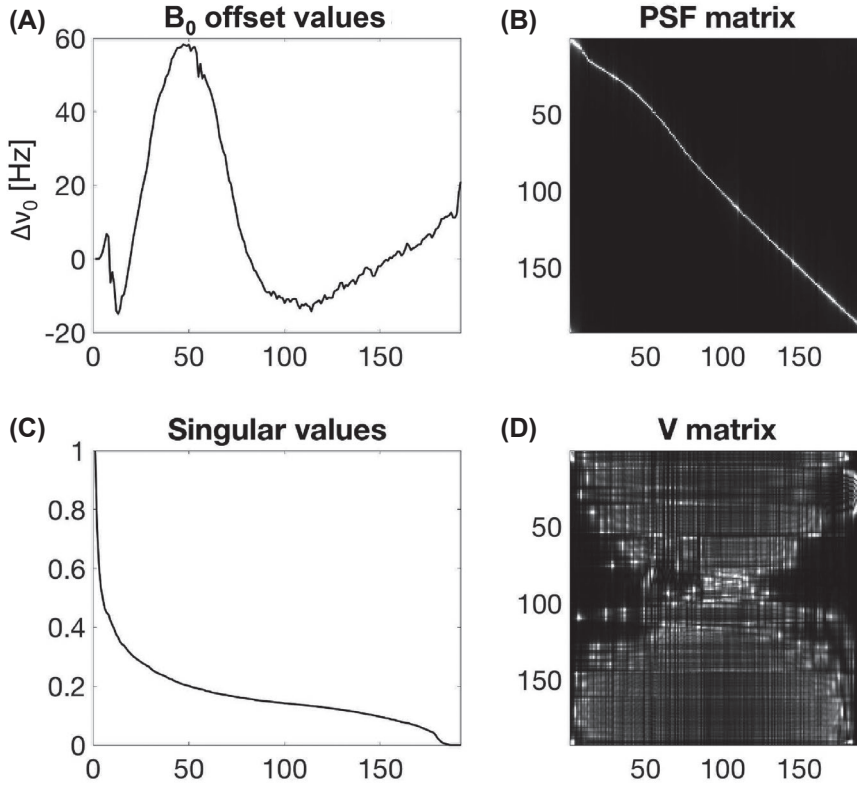
FIGURE 1 Distribution of offset values $\Delta v_{0,n}$ as a function of the voxel index n in a column along the phase-encode (PE) direction obtained experimentally with a multi-echo (ME)-FLASH sequence in the brain of a volunteer (A) and corresponding magnitude of the point-spread function (*PSF*) matrix ($\mathbf{PSF}_{\text{fGE}}^{+}$) for a full-Fourier gradient-echo (fGE)-EPI acquisition with bottom-up trajectory (B). A column of the $\mathbf{PSF}_{\text{fGE}}^{+}$ matrix represents the magnitude of $PSF_{\text{fGE},n}^{+}$ measured at positions $(m-n)$. Also shown are singular values Σ_{nn} (C) and the magnitude of the unitary $\mathbf{V}$ matrix (D) resulting from the singular value decomposition of the $\mathbf{PSF}_{\text{fGE}}^{+}$ matrix

$\Delta v_{0,n}$ values lead to apparent off-diagonal shifts of the center peak in the $\mathbf{PSF}_{\text{fGE}}^{+}$ matrix. An experimental $T_{2,n}^{*}$-column may be constructed in a similar fashion (not shown), with shorter $T_{2,n}^{*}$ values leading to apparent broadening of the center peak.

The least-squares solution of Equation 10 is obtained by the Moore-Penrose pseudo inverse. It can be computed from a singular value decomposition of the **PSF** matrix by decomposing it into a matrix product $\mathbf{U} \cdot \Sigma \cdot \mathbf{V}^{*}$ with $\mathbf{U}$ and $\mathbf{V}$ being unitary matrices. The diagonal matrix Σ contains the singular values (decreasing series of real numbers; Figure 1C). Multiplying the pseudo-inverse, $V \cdot \Sigma^{-1} \cdot U^{*}$, from the left to the image column vector $\tilde{\mathbf{a}}$ yields a distortion-corrected and intensity-corrected representation of the object.

As deconvolutions are often ill-posed and ill-conditioned,[38] noise contributions are amplified, in particular, following inversion of small singular values (ie, due to voxels with low signal intensities increasing the sparsity of $\mathbf{U}$ and $\mathbf{V}$) (Figure 1C,D). Therefore, we applied a smoothing and interpolation procedure to the measured maps,[10] and Tikhonov regularization was integrated by introducing a parameter $\alpha > 0$ in the inversion of the singular values:

$$\Sigma_{nn}^{-1} = \frac{\Sigma_{nn}^{2}}{\Sigma_{nn}^{2} + \alpha} \cdot \frac{1}{\Sigma_{nn}}. \tag{11}$$

This binds the condition number to $\kappa(X) < \left(\sum_{11} / \sum_{nn} \right) \alpha$
.[39]

2.3 | Combination of images acquired with opposite phase blip polarity

While spatially correct coordinates can be straightforwardly reconstructed for a distorted image, this does not necessarily yield a correct intensity distribution. An accurate reconstruction is impossible if information is lost due to compression of signal contributions from different object positions.[20] However, directions of spatial signal shifts depend on the phase-blip polarity: Regions appearing compressed with bottom-up EPI will appear stretched with top-down EPI and vice versa. This provides additional information about the intensity distribution.

In et al[27] presented a procedure for a weighted summation of pairs of PSF_{n}-corrected images acquired with opposite blip polarities to resolve local loss of spatial information due to compression. It can be straightforwardly adapted to combine pairs of DecoDisCo-corrected GRE or SE-EPI acquisitions:

$$\tilde{a}_{m}^{\text{av}} = \frac{\left(\varrho_{m}^{+} \right)^{c} \cdot \tilde{a}_{m}^{+,\text{corr}} + \left(\varrho_{m}^{-} \right)^{c} \cdot \tilde{a}_{m}^{-,\text{corr}}}{\left(\varrho_{m}^{+} \right)^{c} + \left(\varrho_{m}^{-} \right)^{c}}. \tag{12}$$

The weights, $\varrho_{m}^{\pm}$, are further scaled by an empirical exponent c.[27] They are obtained by normalizing the magnitude **PSF** matrices along their columns and calculating the row totals:

$$\varrho_m^{\pm} = \sum_{n=0}^{N_y - 1} \left| PSF_n^{\pm} \left(y_{mn} \right) \right|.$$ (13)

A value of $\varrho_m^{\pm} > 1$ reflects compression during image formation, whereas $\varrho_m^{\pm} < 1$ reflects stretching. To give larger weight to information from originally stretched areas, c is chosen to be negative. The weights can also be computed from the inverse of the **PSF** matrix (ie, the matrix used to correct the images), leading to $c > 0$ as originally used by In et al.[27] For $c = 0$, the combination yields the mean of both contributions with an expected $\sqrt{2}$-fold improvement of the SNR. For $c \to -\infty$, a binary combination is obtained, reflecting the most accurate geometry, although without SNR gain. Other exponents lead to a trade-off between SNR and geometrical accuracy. Note that application of Equation 12 requires acquisition of the whole data set with both blip polarities (sometimes done in dw-MRI, seldom in fMRI).

3 | METHODS

3.1 | Image acquisition

Experiments were performed at 3 T (MAGNETOM Skyra Connectom and MAGNETOM Prisma^{fit}; Siemens Healthcare, Erlangen, Germany) using the body transmit coil and a 32-channel head receive coil. Pulse sequences were implemented under Siemens IDEA and tested with a spherical water phantom (1.25 g $NiSO_4 \cdot 6H_2O$ per kg water). The deconvolutions were evaluated with a 3D-printed phantom (photopolymer) (Figure 2D) filled with an $MnCl_2 \cdot 4H_2O$ solution (61.9 mg per kilogram of water; $T_1 \approx 430$ ms, $T_2^* \approx 27$ ms measured in an unstructured container).[40] Rows of rods (nominal diameters increasing from 1.0 mm to 3.5 mm in steps of 0.25 mm) and two air-filled hollow cylinders for inducing distortions were integrated for evaluating the resolution. To measure PSF_n, a PE table was added to a blipped GRE-EPI
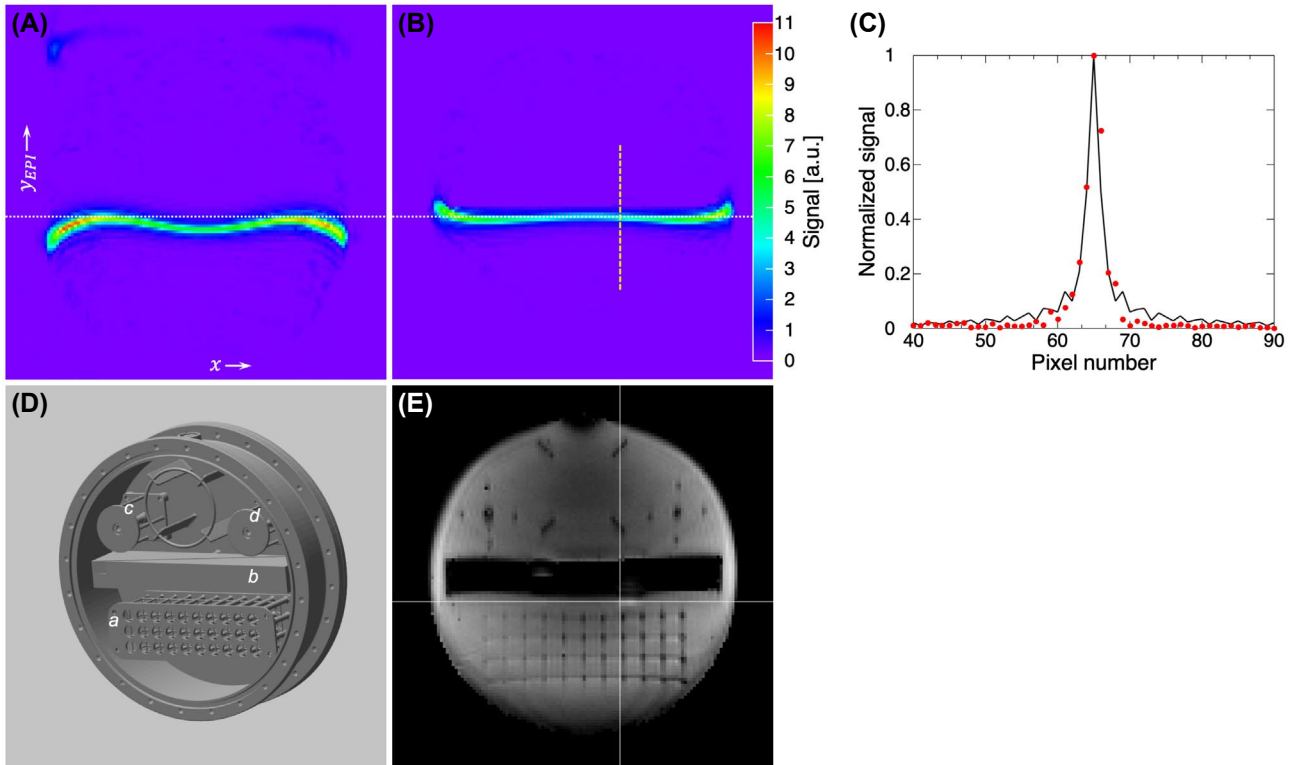
FIGURE 2 Experimental and analytical PSF_n in a resolution phantom. A, Measured PSF (with color-coded intensity a_n) in x-y_{EPI} coordinates, where x is the (undistorted) frequency-encoding (FE) direction and y_{EPI} is the distorted PE direction (the presentation of the PSF map and the notation of coordinates are consistent with Figure 3 of Zaitsev et al[25]). The example corresponds to position $n = 66$ along the undistorted PE direction, which is indicated by a horizontal dotted line. Note the shift of the PSF maximum from this line due to local frequency offsets. B, Application of deconvolution-based distortion correction (DecoDisCo) before the inverse Fourier transform along the PSF dimension realigns the PSF with the dotted line. C, Experimental PSF_n profile (red dots) along the vertical dashed line compared with the profile derived analytically (black solid line) with Equation 3 and $\Delta\nu_{0,n}$, and $T_{2,n}^*$ values measured separately with ME-FLASH. The maxima of both profiles were normalized to 1 for an easier comparison. D, Illustration of the phantom (inner diameter = 154 mm, height = 44 mm) consisting of three rows of 11 rods (diameters increasing from left to right from 1.0 mm to 3.5 mm in steps of 0.25 mm; spacing = 10 mm) (a), a cuboid ($140 \times 30 \times 17$ mm^3) with diagonally opposite slots (2-mm wide, 8-mm deep) in the top and bottom plane (b), and two air-filled hollow cylinders (wall thickness = 1 mm) with inner diameters of 3 mm (c) and 2 mm (d). E, Partial gradient-echo (pGE)-EPI image of the phantom. The horizontal and vertical crosshair lines indicate the position ($n = 66$) of the PSF_n map in (B) and the direction of the profile in (C), respectively
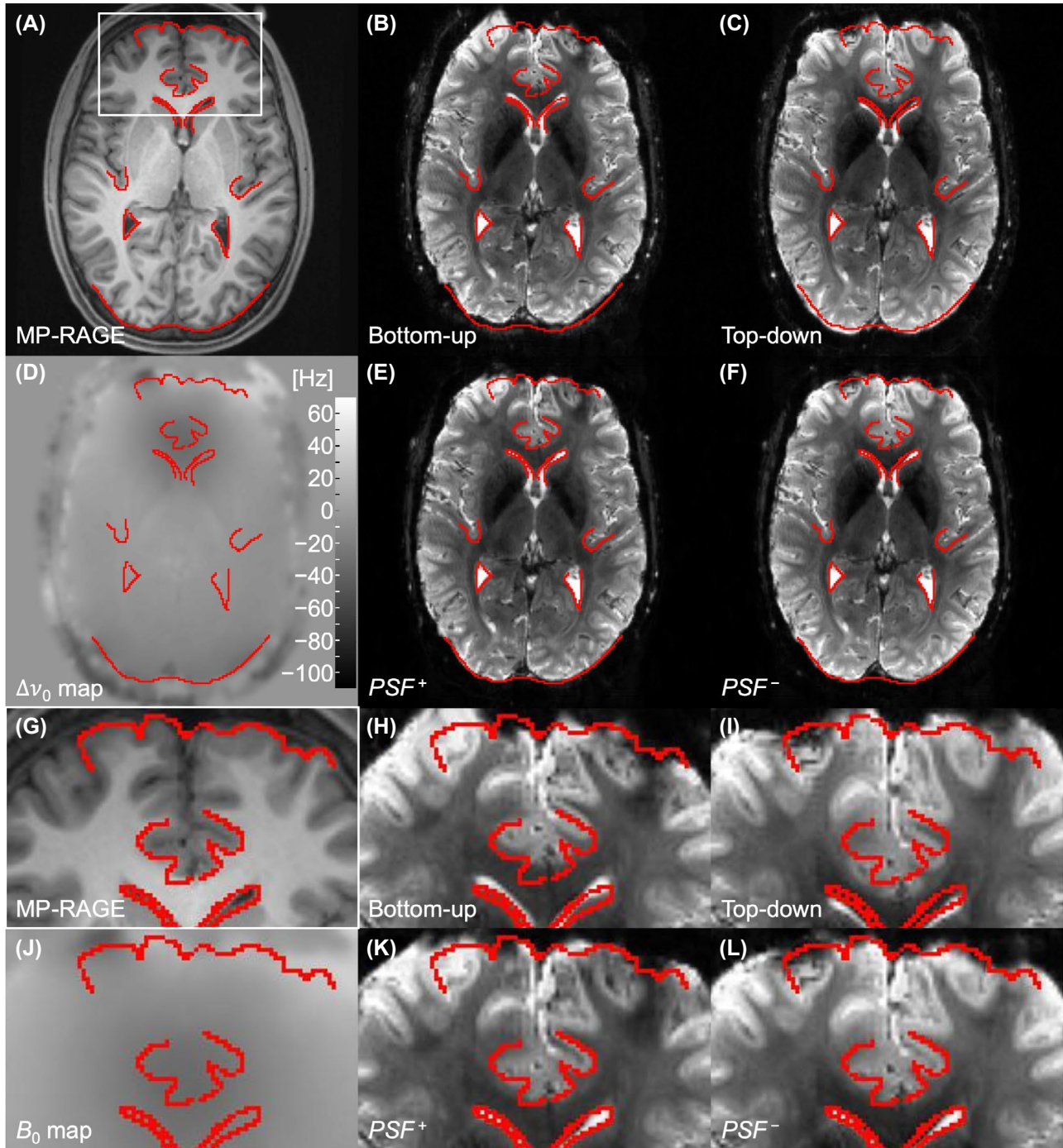
FIGURE 3 Distortion correction of fGE-EPI images (nominal resolution $1.0 \times 1.0 \times 1.3$ mm^3). The upper panel shows a reference MPRAGE image (A), uncorrected bottom-up (B) and top-down (C) EPI images, a $\Delta\nu_0$ map obtained with a separate ME-FLASH acquisition (D), and *PSF*-corrected bottom-up (E) and top-down (F) EPI images. The lower panel (G-L) shows the corresponding enlarged sections from the region indicated by the rectangular box in (A). Red lines indicate arbitrarily chosen anatomical borders on the MPRAGE reference. The value of $T_{2,n}^*$ was arbitrarily set to 50 ms without consideration of spatially specific variations on a voxel level

sequence (TR = 2 seconds, TE = 25 ms, Δy = 1.5 mm, matrix = 128×128, f_p = 5/8) as described by Zaitsev et al.[25] The *PSF* encoding was performed with full resolution (ie, no partial Fourier or parallel imaging were applied along this dimension). Experimental PSF_n maps were extracted after inverse Fourier transform with an optional *PSF* deconvolution step. Distortion and blurring corrections were investigated with fGRE-EPI (TE = 41 ms), pGRE-EPI (TE = 20 ms, f_p = 5/8), and DEPICTING (TE = 4.1 ms). Common parameters of these acquisitions included 24 slices, Δy = 1 mm, matrix = 192×192, TR = 5 seconds, a bandwidth of 1086 Hz/pixel, and 16 or 32 averages.

Following approval by the ethics committee at the Medical Faculty of Leipzig University and after obtaining informed written consent, 6 subjects (1 female, age between 23 and 30 years) participated in the in vivo measurements. For fGE-EPI, 36 slices were recorded with $\Delta y = 1$ mm (matrix $= 192 \times 192$), TR between 5.4 and 6.6 seconds, $TE = 70.8$ ms, and a bandwidth of 930 Hz/pixel. The pGE-EPI or DEPICTING data were recorded with identical slice geometry, $\Delta y = 0.7$ or 1.0 mm (matrix $= 276 \times 276$ or 192×192, respectively), $TR = 5.4$ or 5.7 seconds, $TE = 34.3$ or 4.6 ms, and bandwidths of 755 or 930 Hz/pixel, respectively. In 1 subject, dw-MRI data (pairs of gradient-reversed complex-valued volumes) were recorded as an example of SE-EPI (78 slices, $\Delta y = 1.5$ mm, matrix $= 146 \times 146$, $TR = 5.32$ seconds, $TE = 86$ ms, $R = 2$, and $f_p = 6/8$). Sampling included 60 non-colinear diffusion-weighting directions with b-factors of 1000 s/mm^2 as well as seven scans with $b = 0$. Standard fat suppression was used in all in vivo scans. Ramp sampling and GRAPPA[5] with $R = 3$ (fGE-EPI phantom scans) or $R = 2$ (all other phantom and in vivo scans) were used with all EPI variants. Slice thicknesses were always 1.3 mm or 1.5 mm. The fGE-EPI and pGE-EPI data were acquired separately with both bottom-up and top-down k-space trajectories (without alteration of the readout direction) to evaluate the correction in stretched and compressed regions. Due to the unusually long TE of the fGE-EPI in vivo scans, 16 complex-valued image volumes were recorded and subsequently averaged to increase the SNR for better visualization of small structures. Three-dimensional T_1-weighted anatomical references were acquired in separate sessions using MPRAGE[41] or MP2RAGE[42] imaging.

For obtaining the **PSF** matrix in a geometrically undistorted space, a 2D-ME FLASH sequence[43] was used with 12 bipolar gradient echoes, an interecho time of 1.2 ms or 1.6 ms, and identical slice and resolution parameters as in the GE-EPI and DEPICTING scans. The value of $\Delta v_{0,n}$ was extracted from a linear fit to the unwrapped phases of all echoes. The $T_{2,n}^*$ values were obtained by exponential fitting of the echo magnitudes. Maps of the goodness of fit of both parameters were stored for postprocessing. In selected investigations of T_2^*-related blurring, another ME-FLASH scan was recorded with 24 echoes and 4.5-ms spacing to improve the accuracy of the $T_{2,n}^*$ fits. Unless otherwise noted, GRE-EPI and DEPICTING acquisitions were corrected using the ME-FLASH data, whereas the dw-MRI scan was corrected using $\Delta v_{0,n}$ estimates obtained with TOPUP from the gradient-reversed acquisitions.

3.2 | Image processing

All postprocessing routines were implemented on a standard desktop computer using *MATLAB* (MathWorks, Natick, MA). Voxels of the Δv_0 maps with a goodness of fit smaller than the mean over the slice were labeled as uncertain, and their values were omitted by thresholding or, alternatively, interpolated using discrete cosine transforms. Finally, maps were smoothed using a small Gaussian kernel (FWHM = 2 pixels).

The **PSF** matrices were constructed from cyclically shifted $PSF_n^{\pm}\left(y_{mn}\right)$ with measured input values $\Delta v_{0,n}$ and (optionally) $T_{2,n}^*$. After decomposing the **PSF** matrices using *MATLAB*'s singular value decomposition function, the inversion was performed with variable α. For comparison, the MFR approach[13] was also implemented in *MATLAB*, and TOPUP[20] was used as a stand-alone application.

3.3 | Simulations

For numerical investigations of the combination of pairs of PSF_n-corrected images, synthetic fGE-EPI images were generated using measured image-domain data as input. A forward convolution was applied to the experimental images with a synthetic **PSF** matrix that was obtained using experimental $\Delta v_{0,n}$ values rescaled to $1.5 \cdot \Delta v_{0,n}$ to amplify geometric distortions and $T_2^* \to \infty$ (ie, $R_2^* = 0$) to avoid additional T_2^* related blurring. Complex-valued Gaussian noise (average magnitude of 22% of the average signal magnitude of the masked brain region) was added, and a regularized *PSF* deconvolution ($\alpha = 0.01$) was applied. The corrected image pairs with opposite blip polarities were combined using Equation 12 with different settings of c.

4 | RESULTS

Distortions were evaluated separately for fGE-EPI and pGE-EPI. Similarly, partial Fourier and T_2^* effects were evaluated separately. Unless otherwise noted, voxel-specific corrections of T_2^* effects were omitted by arbitrarily setting $T_{2,n}^* = 50$ ms, a typical (uncorrected) value in cortical gray matter at 3 T.[44-46]

4.1 | Comparison of experimental and analytical *PSF*

The PSF_n mapping yielded a position-dependent shift of the experimental *PSF* due to local frequency offsets (Figure 2A). Application of DecoDisCo with a separately recorded Δv_0 map aligned the PSF at the correct position in undistorted PE direction (Figure 2B). Note that T_2^*-related blurring was not corrected here. A remaining deviation from the undistorted position is visible at the edges, resulting from less accurate frequency offset estimates at the phantom border (Figure 2E).

Profiles of the experimental and analytical PSF showed excellent agreement in the central part, whereas the weak oscillatory pattern due to the partial-Fourier reconstruction with zero filling was smoothed in the experimental PSF (Figure 2C). This might be related to the scanner implementation of the parallel-imaging reconstruction.

4.2 | Correction of distortions in full-Fourier and partial-Fourier GE-EPI

Figure 3 shows high-resolution fGE-EPI images and a corresponding $\Delta\nu_0$ map. The comparison with the MPRAGE image (Figure 3A) demonstrates that distortions on the uncorrected EPI images (Figure 3B,C,H,I) have expected opposite directions for inverted PE directions. Good agreement of the two corrected EPI images is obtained after *PSF* deconvolution (Figure 3E,F,K,L). Both results agree well with the reference, indicating sufficient accuracy for correcting high-resolution EPI images.

Applications to pGE-EPI are presented in Figure 4. Note that typical partial-Fourier reconstruction algorithms, such as the homodyne[47] or the projection onto convex set[48] techniques, use assumptions on the phase evolution extracted from the symmetrically acquired portion of k-space data. As their exact scanner implementations were not available, we used simpler k-space filling techniques during image reconstruction for a proof of concept: (1) zero filling (ie, missing k-space data filled with zeroes) (Equation 3) and (2) conjugate filling (Equation 6). No assumptions about the phase were made in Equation 6, and no additional convolutions were applied to avoid typical errors in partial-Fourier reconstructions.[49] Compared with the reference (Figure 4A), DecoDisCo achieved similar distortion corrections with zero and conjugate filling (Figure 4C,F). However, sharper images (ie, reduced blurring) were obtained with conjugate filling (Figure 4F). For further evaluation, we simulated exponential signal decays with T_2^* values of brain tissue and partial-Fourier sampling. Increased blurring exceeding T_2^* effects resulted after decreasing f_p, due to the shortened effective acquisition window $(f_p \cdot N_y \cdot \Delta t_e)$ and correspondingly higher level of truncation with zero filling (data not shown).

4.3 | Correction of distortions in double-shot center-out EPI

Intensity errors occur in distorted images if multiple voxels are mapped onto the same location. As DEPICTING uses a segmented acquisition with opposite blip polarity, frequency offsets lead to opposite voxel shifts for the two tiles, and the *PSF* shows a double-peak pattern.[37] Therefore, DEPICTING is more prone to intensity errors than standard EPI. The very short *TE* achieved with its center-out trajectory yields high signal intensities with minimal phase evolution. Consequently, constructive interferences of shifted signal
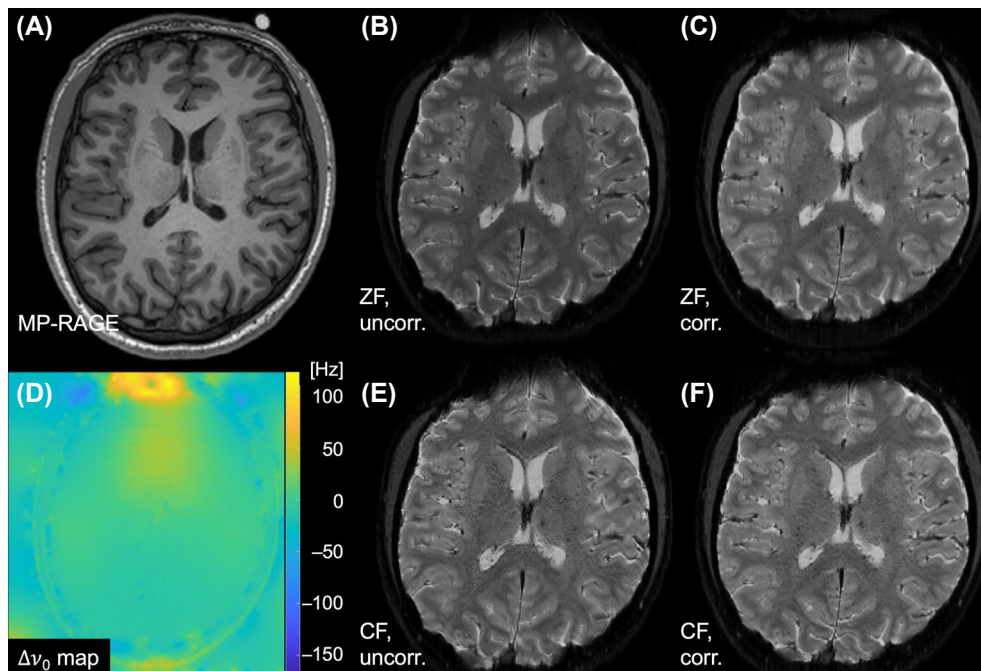
FIGURE 4 Distortion correction of pGE-EPI images (nominal spatial resolution $0.7 \times 0.7 \times 1.3$ mm^3 and $f_p = 5/8$). The top row shows a reference MPRAGE image (A) as well as uncorrected (B) and corrected (C) images with zero-filling (ZF) of missing k-space data. The bottom row shows a $\Delta\nu_0$ map obtained with a separate ME-FLASH acquisition (D) as well as uncorrected (E) and corrected (F) images with conjugate filling (CF) of missing k-space data. The value of $T_{2,n}^*$ was arbitrarily set to 50 ms without consideration of spatially specific variations

contributions produce characteristic hyperintensities. These images are particularly suited to evaluate the intensity distribution obtained after distortion correction. Figure 5 demonstrates that both the MFR and DecoDisCo restored the right brain shape. Spurious hyperintensities (indicated by arrows) remained after MFR (Figure 5C,G), whereas DecoDisCo partly restored piled-up signal (Figure 5D,H). These regions contain contributions of a corrected intensity distribution from previous voxel stretching plus a smeared average intensity from previous voxel compression. The improved intensity distribution might improve co-registration results.

## 4.4 | Evaluation of T_2^*-related blurring

Acquisitions with fGE-EPI, pGE-EPI (with zero filling), and DEPICTING in the resolution phantom are compared in Figure 6. Uncorrected images (Figure 6A-C) showed substantial distortions (appearing as double contours with DEPICTING), which were corrected with MFR (Figure 6E-G) or DecoDisCo and $\Delta\nu_0$ maps (Figure 6H-J; no consideration of T_2^*). Unrecovered signal voids due to signal compression appeared in regions affected by strong susceptibility gradients (regions of interest 1, 2, and 4 with fGE-EPI and pGE-EPI; regions of interest 1 and 4 with DEPICTING).

While the differently sized rods appeared sharp with fGE-EPI, substantial and moderate blurring (along PE direction) was found with pGE-EPI and DEPICTING, respectively (Figure 6E-J). Deblurring by consideration of T_2^* maps had only minor effects for fGE- and pGE-EPI, but improved the sharpness of DEPICTING images (Figure 6K-M; compare also profiles in Supporting Information Figure S1).

Figure 7 demonstrates corrections of T_2^*-induced blurring in fGRE-EPI in vivo acquisitions. As a zeroth-order approximation for T_2^* deblurring, spatially uniform T_2^* maps (with different T_2^* values between 10 ms and 80 ms) were assumed in the in vivo example, yielding already a sufficient level of correction obtained with $T_2^* \geq 40$ ms in most brain regions.

4.5 | Combination of EPI scans with opposite blip polarity

Despite good general agreement of the corrected bottom-up and top-down images (see Figure 3E,F,K,L), the signal differed for different blip polarities, especially in areas of large $\Delta\nu_{0,n}$. Figure 8A shows one-dimensional profiles of simulated top-down and bottom-up fGRE-EPI acquisitions after PSF_n correction (red and blue solid lines, respectively) in comparison to the undistorted input object (black dashed
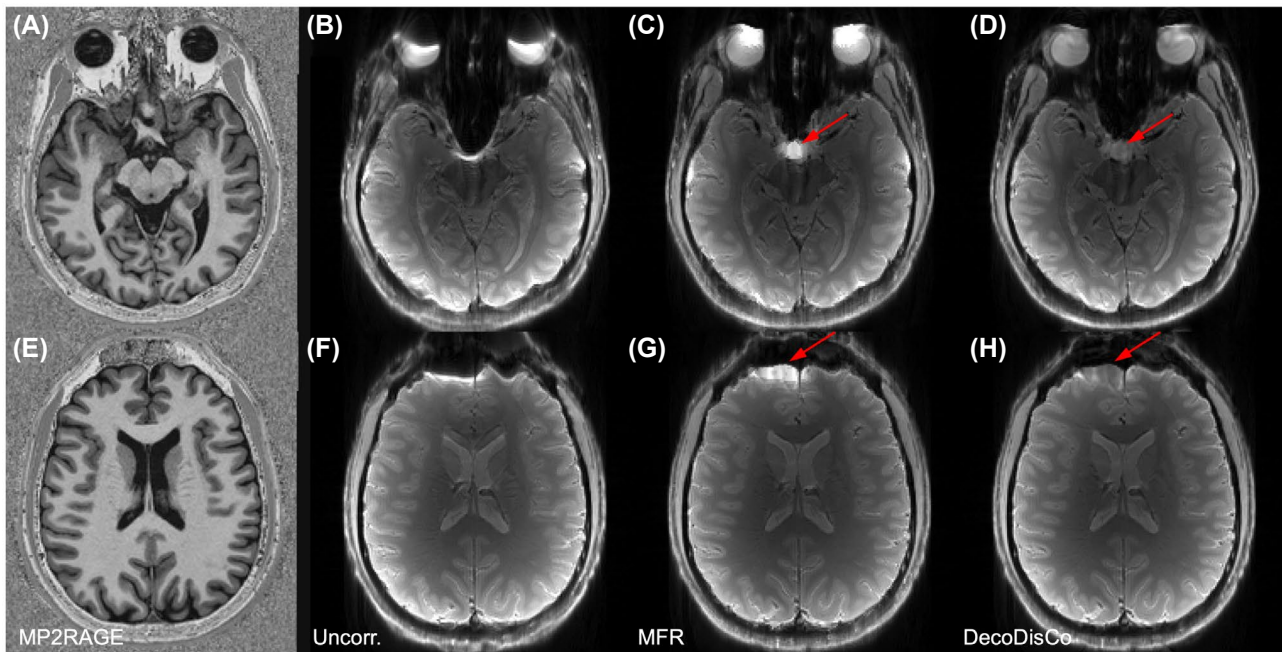

FIGURE 5 Demonstration of the inherent intensity correction of the *PSF* deconvolution method. B,F, Uncorrected axial double-shot EPI with center-out trajectories and intrinsic navigation (DEPICTING) acquisitions (ie, double-shot center-out GRE-EPI trajectories sampled with very short *TE* of 4.6 ms) at different levels through the brain demonstrating both geometric distortions along the PE direction (anterior–posterior) in comparison to MP2RAGE reference images (A,E) as well as hyperintensities. C,G, Results obtained with a multifrequency reconstruction (MFR) that achieves distortion correction but fails to correct the hyperintensities. D,H, Results obtained with DecoDisCo with slightly superior distortion correction as well as an improved intensity profile (arrows). Both the MRF and DecoDisCo used the same $\Delta\nu_0$ map, which was obtained with a separate ME-FLASH acquisition. The value of $T_{2,n}^*$ was arbitrarily set to 50 ms without consideration of spatially specific variations
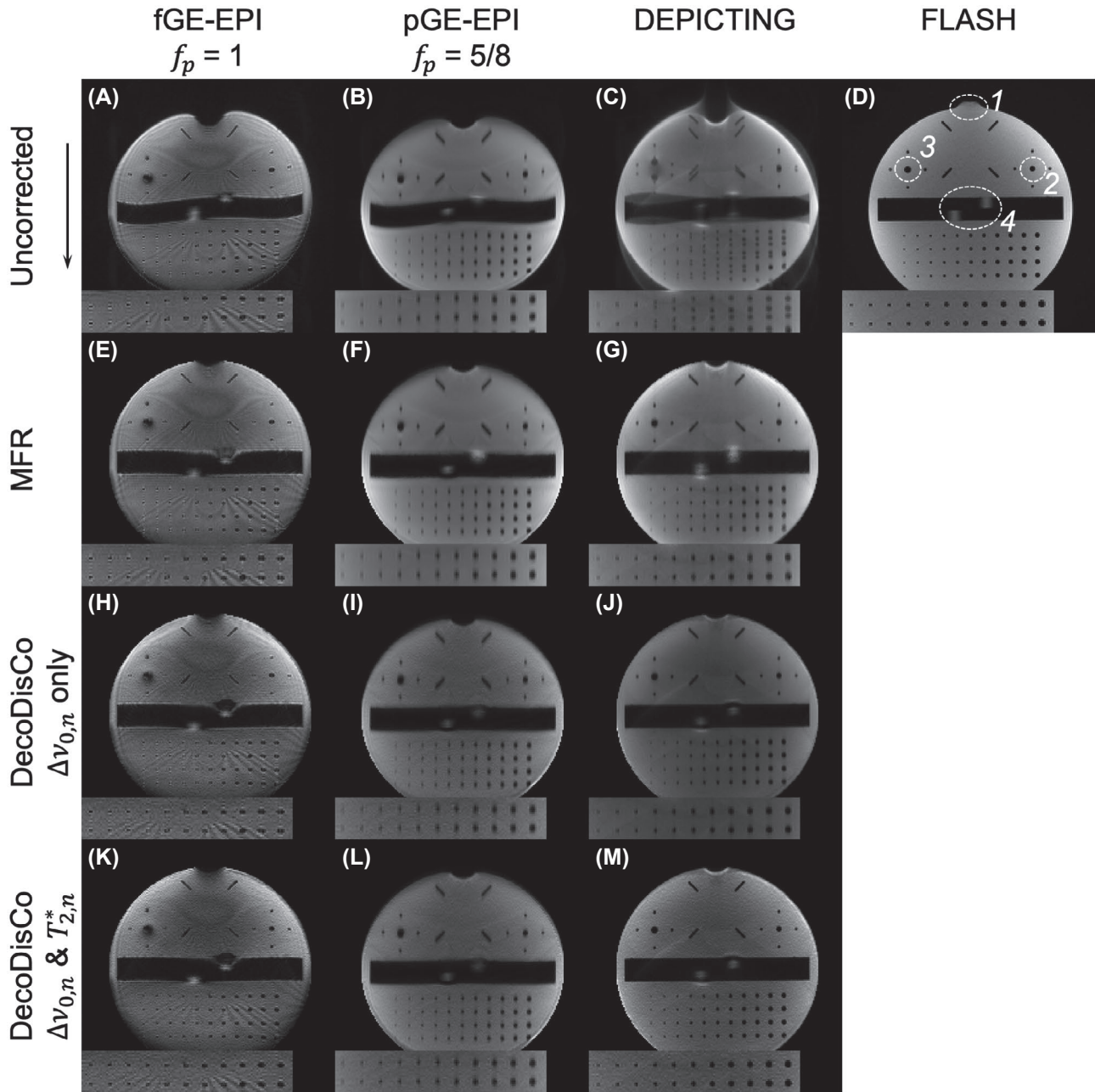
FIGURE 6 Acquisitions in the resolution phantom with fGE-EPI (A,E,H,K), pGE-EPI (B,F,I,L), and DEPICTING (C,G,J,M). The black arrow indicates the PE direction used for the fGE-EPI and pGE-EPI scans. Besides the uncorrected (A-C) and MFR-corrected images (E-G), DecoDisCo corrections of frequency offsets without (ie, setting $T_2^* \to \infty$) (H-J) and with additional consideration of T_2^* effects (K-M) are shown in comparison to a FLASH reference (D). Rectangular inserts show the same zoomed region at the level of the upper two rows of solid photopolymer cylinders (diameters decreasing linearly from left to right from 3.5 mm to 1 mm). Additional intensity profiles along the PE direction at the position of the rods are presented in Supporting Information Figure S1. Note that different ME-FLASH acquisitions (echo spacings of 1.2 ms and 4.5 ms, respectively) were used for Δv_0 and T_2^* mapping in these experiments. The following regions of interest (ROIs) are indicated on the FLASH image: ROI 1, filler opening; ROIs 2 and 3, air-filled hollow cylinders (3-mm and 2-mm inner diameter, respectively); and ROI 4, 8-mm deep slots in the top and bottom plane of the central cuboid

line). Combined profiles obtained with Equation 12 are shown in Figure 8C. Three different c values were considered (Figure 8B). Only minor differences were observed for the weighted ($c = -4$) and the either/or binary combination, whereas for the arithmetic mean ($c = 0$), a larger deviation from the input profile is evident, particularly in the left part.

Corresponding 2D images are shown in Figure 9. Red arrows in the uncombined images indicate areas that were not accurately reconstructed due to signal compression. These artifacts are also visible, with reduced intensity, in the combined image corresponding to the arithmetic mean (Figure 9D). They are mitigated for $c \neq 0$, which yields an improved signal
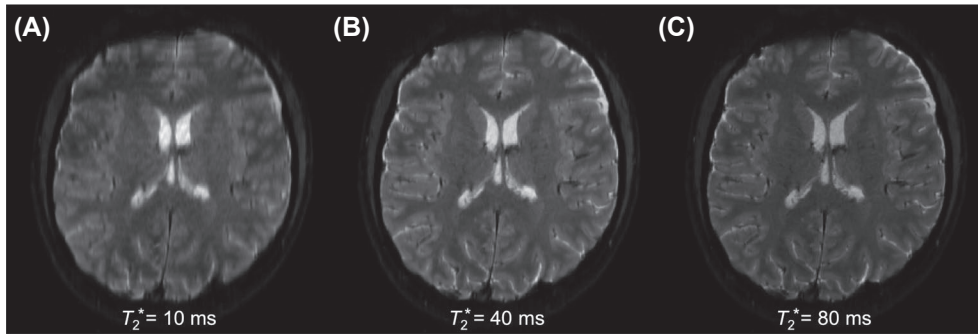
FIGURE 7 First-order corrections of image blurring due to T_2^* relaxation (fGE-EPI acquisitions). Instead of an experimental map of the local relaxation time, uniform T_2^* values of 10 ms (A), 40 ms (B), and 80 ms (C) were assumed in the deconvolutions. Sharper reconstructions result with T_2^* values matching the T_2^* of gray matter

distribution. The choice of $c = -4$ yielded a reduced noise level and the lowest mean square error.

4.6 | Combination of DecoDisCo and TOPUP

Deconvolutions tend to create oversharpened images due to the inversion of noise, which requires additional regularization in comparison to a convolution-based voxel-shift used with TOPUP. A combination of the two methods may therefore result in sharper images without the need to measure a field map: If acquisitions with opposite blip polarities are available (as often performed in dw-MRI), an estimate of the underlying field map may be generated with TOPUP. Subsequently, distortion correction and pair-wise (weighted) combination of PSF_n-corrected images may be performed with DecoDisCo. An example applied to SE-EPI with and without diffusion weighting is shown in Figure 10. Geometric distortions were corrected by achieving increased similarity of acquisitions with opposite gradient polarities (Figure 10, DecoDisCo). The combined images (here $c = -2$) were superior to the individually corrected images, suggesting that spatial accuracy is gained from the combination. A comparison to TOPUP corrections with the "least-squares restoration" mode yielded similar performance of both approaches, which were based on the same underlying field map. Visual inspection did not indicate different sharpness of the conjugate-filling reconstruction ($f_p = 6/8$) over the TOPUP result.

5 | DISCUSSION

A versatile procedure is introduced to correct geometric distortions in EPI-type acquisitions. It is based on an analytical model of the PSF, a preparation scan to acquire maps of the local B_0 (eg, with multiple-PE or ME methods) and (optionally) T_2^* distributions as input parameters, and a regularized PSF deconvolution.

Strong gradients of $\Delta\nu_{0,n}$ lead to insignificant rows in the PSF matrix, whereas short $T_{2,n}^*$ values result in insignificant columns. These effects decrease the conditioning of the system, which requires regularization of the inversion. Thikonov regularization with α, depending on the acquisition scheme and noise level, improved the conditioning sufficiently to yield noncorrupted images.

Interestingly, the double-peak pattern of the DEPICTING PSF (Equation 8) also improved the conditioning of the associated inversion problem, as the corresponding **PSF** matrix is the sum of two (half-Fourier GE-EPI) PSFs of opposite blip polarity. This yields additional information, which may be exploited in future work for an improved reconstruction.[50] Due to multiple-to-one mappings, specific image regions may not be reconstructed correctly if only acquisitions with a single blip polarity are available. Combined GE-EPI or SE-EPI acquisitions with opposite polarity achieve improved corrections, as demonstrated with the adaptation of a previously published scheme for a weighted summation.[27] A potential advantage of DecoDisCo is that experimental mapping is not required, thus avoiding, for example, flow artifacts from CSF or ghosting, which may affect the measured PSF.

Evaluation of the deblurring efficiency requires careful consideration of the imaging readout.[51] With fGE-EPI, high spatial frequencies carrying information about fine structures are acquired early (ie, with minimal T_2^*-weighting) at one edge of k-space, but late at the other edge (ie, with maximal T_2^*-weighting). Despite the signal decay during the readout, information on high spatial frequencies (ie, information on "sharpness") is available from the initially acquired k-space lines, which efficiently mitigates related blurring. Consequently, further deblurring is relatively inefficient. This is not a limitation of the method, but more an intrinsic advantage of the well-posed conditions of fGE-EPI. With pGE-EPI (and, particularly, with small), high spatial frequencies are acquired late. Hence, no compensating information is available from the other k-space half, leading to degraded sharpness of partial-Fourier acquisitions (in particular, with zero-filling reconstructions). Of note, the full complex PSF is required to characterize this specific
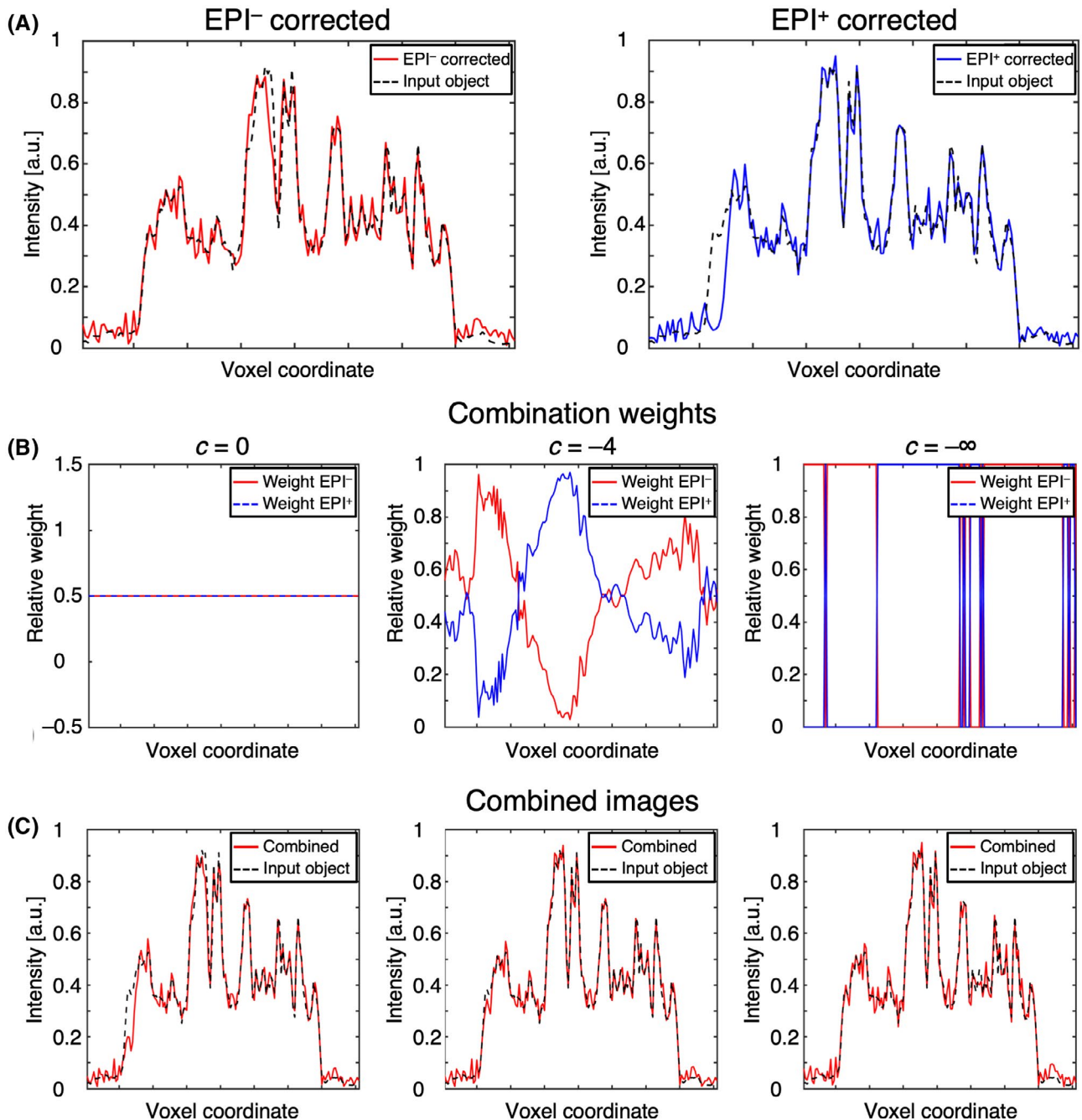
FIGURE 8 Results from combining synthetic PSF-based distortion-corrected fGE-EPI images acquired with opposite PE directions (one-dimensional profiles through the slices shown in Figure 9). Red and blue solid lines indicate corrected profiles obtained with top-down ("EPI⁻") and bottom-up ("EPI⁺") trajectories. Dashed black lines indicate the undistorted input. In addition to profiles of corrected single acquisitions (A), results from weighted summations (C) with different exponents ($c = 0$ [left], $c = -4$ [middle], and $c \to -\infty$ [right]), as well as the corresponding combination weights (B), are presented. The mean squared errors (MSEs) of these profiles with respect to the input are 0.56, 0.35, and 0.44, respectively

contribution to blurring, whereas a restriction to the magnitude as used in earlier discussions of pGE-EPI[35,37,52,53] is inadequate.[51] With DEPICTING, the entire k-space is acquired (albeit in two tiles), mitigating the specific loss of sharpness associated with pGE-EPI and zero filling. However, both k-space edges are sampled after significant relaxation. This specific T_2^*-related blurring can be corrected with DecoDisCo if a sufficiently accurate map is available.

Motion producing an inconsistent field-map estimate, field drifts, or higher-order field variations were not considered in the mathematical model and, hence, remain as potential sources of image artifacts. For example, respiration-induced dynamic field changes were shown to produce dynamic changes.[54,55] These are general limitations of static correction methods[37] and not specific to DecoDisCo. Such effects may be addressed by integrating prospective motion correction[56] or information
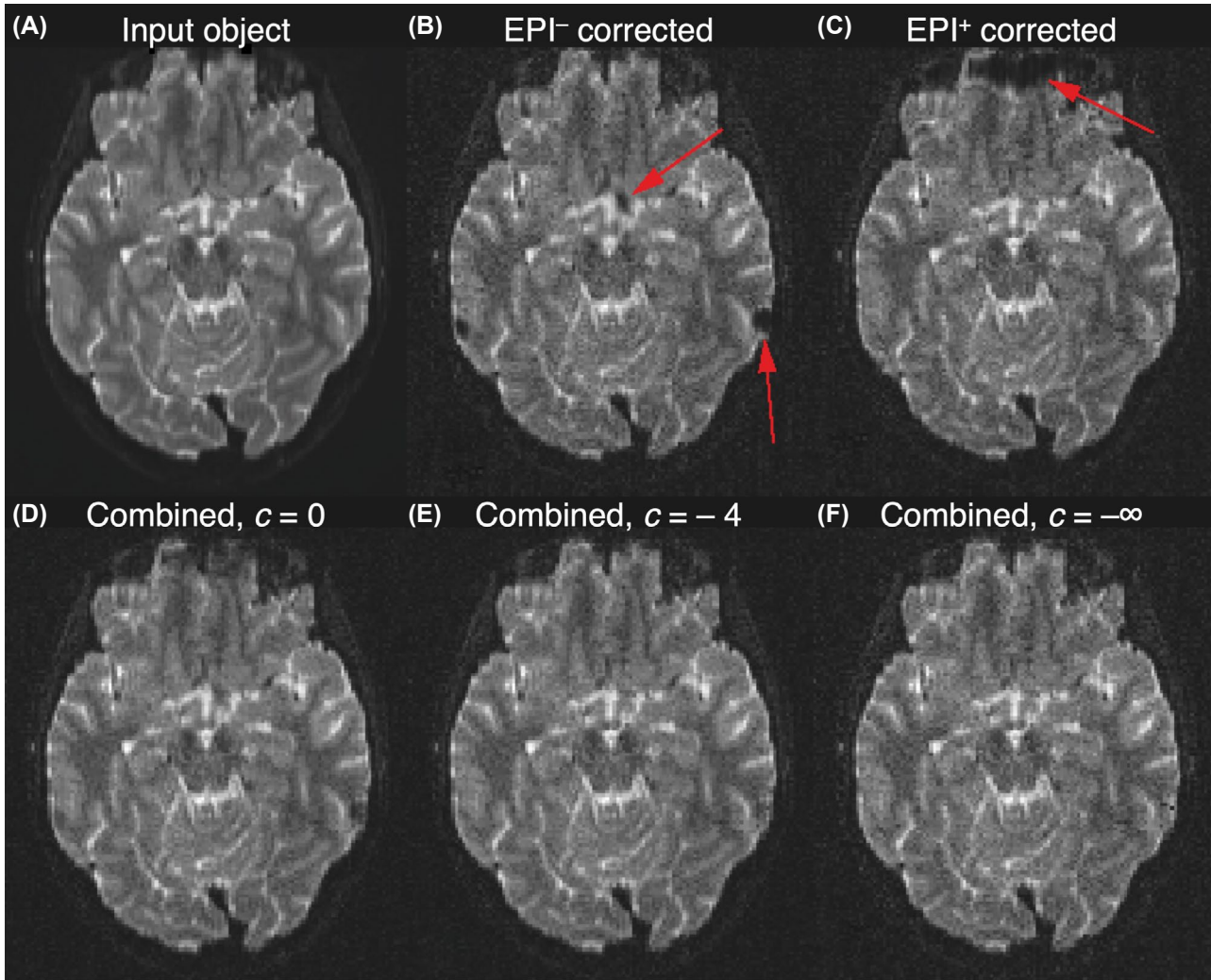
FIGURE 9 Results from combining synthetic PSF-based distortion-corrected fGE-EPI images acquired with opposite PE directions (2D slices corresponding to the profiles shown in Figure 8). In addition to the input image (A) and the corrected single acquisitions with top-down (B) and bottom-up trajectories (C), results from weighted summations with different exponents ($c=0$ [D], $c=-4$ [E], and $c\to-\infty$ [F]) are also presented. B,C, Areas that are not sufficiently corrected due to signal compression are indicated by red arrows. This information is (partly) recovered in weighted summations with $c\neq0$. Weighted averaging with $c=-4$ (empirically obtained) yielded a smaller MSE than with $c=0$ (5.52 vs 6.17, respectively), whereas a larger MSE (7.36) resulted with $c\to-\infty$ due to the higher noise level in the binary combination

obtained with a dynamic field camera.[57] Additionally, GE-EPI acquisitions with opposite blip polarities might be differently modulated by variations of the effective induced by echo shifting.[58,59] This might lower the accuracy of a pairwise combination of PSF_n-corrected images. In dw-MRI, only a single pair of non-dw acquisitions with reversed PE is, in general, sufficient for obtaining a field map, which might be used to correct all dw data. A potential challenge is the shot-to-shot phase instability of acquisitions using strong diffusion-weighting gradients. Although previous work has shown that sophisticated phase correction is possible even under such conditions,[60] this strategy requires future investigations.

In our approach, T_2^* relaxation is modeled as a monoexponential decay. This is likely an oversimplification due to partial-volume effects or combined local and long-range contributions to the field distribution inside a voxel. More complex descriptions of the signal decay have been published (eg, Refs. 45,46,61), suggesting potential adaptation of the PSF. However, the results from Figure 7 demonstrate that T_2^*-related blurring can already be mitigated by assuming a uniform T_2^* according to the longest T_2^* (or longer) of the image volume. In our experiments, values of 40-50 ms served as a reasonable approximation for expected gray-matter values in the human brain at 3 T.[45,46]

Comparing DecoDisCo with other distortion corrections, we note that the MFR technique also requires a separate field-map acquisition. In our experiments, the PSF-based corrections recovered more image details than an MFR with substantially reduced intensity artifacts (Figure 5). On the other hand, the MFR is universally applicable to any k-space trajectory without further adaptation, whereas an analytical approximation of the PSF must be derived for DecoDisCo.
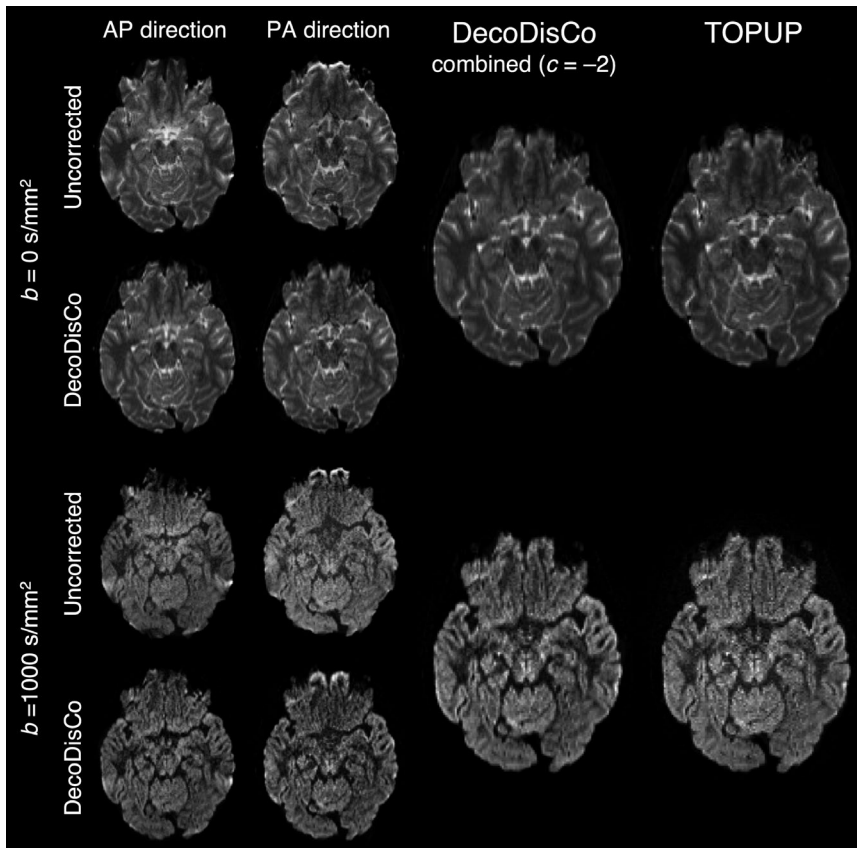
FIGURE 10 Application of DecoDisCo to diffusion-weighted spin-echo EPI. Images were acquired with opposite phase-blip polarities using anterior–posterior (AP; first column) and posterior–anterior (PA; second column) PE direction without ($b = 0$ s/mm^2; top panel) and with diffusion weighting ($b = 1000$ s/mm^2; bottom panel). The field map was estimated with TOPUP. For both b-values, successful correction of geometric distortions is evident from the increased similarity of images acquired with the different PE directions, although residual differences remain in heavily distorted regions (in particular, in frontal regions affected by signal compression). The weighted combination ($c = -2$) of both acquisitions (third column) suggests a superior image quality in these regions. Results obtained with TOPUP (fourth column) are also shown for comparison

TOPUP is a popular method for an offline field-map estimation. It relies on a more heuristic algorithm, aiming at mapping pairs of gradient-reversed images onto each other. This cannot correct multiple-to-one mappings. In principle, it can be beneficial to combine multiple-PE field-map estimation methods and *PSF*-based deconvolution to obtain a first-order estimate of the field map based on simplifying assumptions.

Whereas conventional EPI-based neuroimaging (in particular, routine fMRI) is often performed at relatively low resolution and involves spatial smoothing, EPI resolution is critical in specific applications including laminar fMRI,[6,8] fast quantitative susceptibility mapping,[62,63] or high-resolution dw-MRI.[60,64] Such areas of increasing current interest require high-quality distortion correction. Further experimental evaluation of potential benefits from additional deblurring is therefore warranted.

6 | CONCLUSIONS

We have shown that distortion correction of EPI acquisitions is feasible by deconvolution in image space following proper regularization. The analytic approach intrinsically corrects T_2^*-related blurring and intensity artifacts in addition to geometrical distortions. The method is applicable in combination with different field-mapping techniques, namely ME-FLASH or TOPUP, with overall improved image quality.

DATA AVAILABILITY STATEMENT
The *MATLAB* code and example data that support the findings of this study are openly available at https://github.com/nmr-unit/DecoDisCo. Full-resolution STL files of the resolution phantom are openly available at https://dataverse.harvard.edu/dataset.xhtml?persistentId=doi:10.7910/DVN/PCQHP9.

ORCID
Harald E. Möller https://orcid.org/0000-0002-5659-1925

TWITTER
Harald E. Möller @HaraldMoeller

REFERENCES
1. Mansfield P. Multi-planar image formation using NMR spin echoes. *J Phys C: Solid State Phys*. 1977;10:L55-L58.
2. Schmitt F, Stehling MK, Turner R, eds. *Echo-Planar Imaging. Theory, Technique and Application*. Berlin: Springer; 1998:662.
3. Jezzard P, Clare S. Sources of distortions in functional MRI data. *Hum Brain Mapp*. 1999;8:80-85.

4. Pruessmann KP, Weiger M, Scheidegger MB, Boesiger P. SENSE: sensitivity encoding for fast MRI. *Magn Reson Med*. 1999;42:952-962.

5. Griswold MA, Jakob PM, Heidemann RM, et al. Generalized autocalibrating partially parallel acquisitions (GRAPPA). *Magn Reson Med*. 2002;47:1202-1210.

6. Huber L, Goense J, Kennerley AJ, et al. Cortical lamina-dependent blood volume changes in human brain at 7 T. *Neuroimage*. 2015;107:23-33.

7. Guidi M, Huber L, Lampe L, Gauthier CJ, Möller HE. Lamina-dependent calibrated BOLD response in human primary motor cortex. *Neuroimage*. 2016;141:250-261.

8. Huber L, Uludag K, Möller HE. Non-BOLD contrast for laminar fMRI in humans: CBF, CBV, and CMR_{O2}. *Neuroimage*. 2019;195:742-760.

9. Studholme C, Constable RT, Duncan JS. Accurate alignment of functional EPI data to anatomic MRI using a physics-based distortion model. *IEEE Trans Med Imaging*. 2000;19:1115-1127.

10. Jezzard P, Balaban RS. Correction for geometric distortion in echo planar images from B0 field variations. *Magn Reson Med*. 1995;34:65-73.

11. Chen N-K, Wyrwicz AM. Correction for EPI distortions using multi-echo gradient-echo imaging. *Magn Reson Med*. 1999;41:1206-1213.

12. Maeda A, Sano K, Yokoyama T. Reconstruction by weighted correlation for MRI with time-varying gradients. *IEEE Trans Med Imaging*. 1988;7:26-31.

13. Noll DC, Meyer CH, Pauly JM, Nishimura DG, Macovski A. A homogeneity correction method for magnetic resonance imaging with time-varying gradients. *IEEE Trans Med Imaging*. 1991;10:629-637.

14. Man L-C, Pauly JM, Macovski A. Multifrequency interpolation for fast off-resonance correction. *Magn Reson Med*. 1997;37:785-792.

15. Chen N-K, Oshio K, Panych LP. Application of k-space energy spectrum analysis to susceptibility field mapping and distortion correction in gradient-echo EPI. *Neuroimage*. 2006;31:609-622.

16. Chang H, Fitzpatrick JM. A technique for accurate magnetic resonance imaging in the presence of field inhomogeneities. *IEEE Trans Med Imaging*. 1992;11:319-329.

17. Morgan PS, Bowtell RW, McIntyre DJO, Worthington BS. Correction of spatial distortion in EPI due to inhomogeneous static magnetic fields using the reversed gradient method. *J Magn Reson Imaging*. 2004;19:499-507.

18. Weiskopf N, Klose U, Birbaumer N, Mathiak K. Single-shot compensation of image distortions and BOLD contrast optimization using multi-echo EPI for real-time fMRI. *Neuroimage*. 2005;24:1068-1079.

19. Andersson JLR, Skare S. A model-based method for retrospective correction of geometric distortions in diffusion-weighted EPI. *Neuroimage*. 2002;16:177-199.

20. Andersson JLR, Skare S, Ashburner J. How to correct susceptibility distortions in spin-echo echo-planar images: application to diffusion tensor imaging. *Neuroimage*. 2003;20:870-888.

21. Jenkinson M, Beckmann CF, Behrens TEJ, Woolrich MW, Smith SM. FSL. *Neuroimage*. 2012;62:782-790.

22. Graham MS, Drobnjak I, Jenkinson M, Zhang H. Quantitative assessment of the susceptibility artefact and its interaction with motion in diffusion MRI. *PLoS One*. 2017;12:e0185647.

23. Robson MD, Gore JC, Constable RT. Measurement of the point spread function in MRI using constant time imaging. *Magn Reson Med*. 1997;38:733-740.

24. Zeng H, Constable RT. Image distortion correction in EPI: comparison of field mapping with point spread function mapping. *Magn Reson Med*. 2002;48:137-146.

25. Zaitsev M, Hennig J, Speck O. Point spread function mapping with parallel imaging techniques and high acceleration factors: fast, robust, and flexible method for echo-planar imaging distortion correction. *Magn Reson Med*. 2004;52:1156-1166.

26. Chung J-Y, In M-H, Oh S-H, Zaitsev M, Speck O, Cho Z-H. An improved PSF mapping method for EPI distortion correction in human brain at ultra-high field (7T). *Magn Reson Mater Phy*. 2011;24:179-190.

27. In M-H, Posnansky O, Beall EB, Lowe MJ, Speck O. Distortion correction in EPI using an extended PSF method with a reversed phase gradient approach. *PLoS One*. 2015;10:e0116320.

28. Marques JP, Bowtell RW. Evaluation of a new method to correct the effects of motion-induced B_0-field variation during fMRI. In: Proceedings of the 13th Annual Meeting of ISMRM, Miami Beach, Florida, 2005. p 510.

29. Lamberton F, Delcroix N, Grenier D, Mazoyer B, Joliot M. A new EPI-based dynamic field mapping method: application to retrospective geometrical distortion corrections. *J Magn Reson Imaging*. 2007;26:747-755.

30. Visser E, Poser BA, Marth M, Zwiers MP. Reference-free unwarping of EPI data using dynamic off-resonance correction with multiecho acquisition (DOCMA). *Magn Reson Med*. 2012;68:1247-1254.

31. Dymerska B, Poser BA, Barth M, Trattnig S, Robinson SD. A method for the dynamic correction of B0-related distortions in single-echo EPI at 7 T. *Neuroimage*. 2018;168:321-331.

32. Patzig F, Mildner T, Möller HE. Correction of susceptibility-related image distortion based on an analytic point-spread function. In: Proceedings of the 25th Annual Meeting of ISMRM, Honolulu, Hawaii, 2017. p 573.

33. Liang Z-P, Lauterbur PC. *Principles of Magnetic Resonance Imaging. A Signal Processing Perspective*. Piscataway, NJ: IEEE Press; 2000:416.

34. Möller HE, Bossoni L, Connor JR, et al. Iron, myelin, and the brain: neuroimaging meets neurobiology. *Trends Neurosci*. 2019;42:384-401.

35. Brown RW, Cheng Y-CN, Haacke EM, Thompson MR, Venkatesan R. *Magnetic Resonance Imaging: Physical Principles and Sequence Design*. Hoboken, NJ: John Wiley & Sons; 2014:944.

36. Feinberg DA, Hale JD, Watts JC, Kaufman L, Mark A. Halving MR imaging time by conjugation: demonstration at 3.5 kG. *Radiology*. 1986;161:527-531.

37. Hetzer S, Mildner T, Möller HE. A modified EPI sequence for high-resolution imaging at ultra-short echo time. *Magn Reson Med*. 2011;65:165-175.

38. Hadamard J. Sur les problèmes aux dérivées partielles et leur signification physique. *Princeton Univ Bull*. 1902;13:49-52.

39. Engl HW, Hanke M, Neubauer A. *Regularization of Inverse Problems*. Dordrecht: Kluwer Academic Publishers; 2000:322.

40. Müller R, Mildner T, Schlumm T, Patzig F, Möller HE. Modular 3D-printable resolution phantom for magnetic resonance imaging. *Harvard Dataverse*. 2020. https://doi.org/10.7910/DVN/PCQHP9

41. Mugler JP, Brookeman JR. Three-dimensional magnetization-prepared rapid gradient-echo imaging (3D MP RAGE). *Magn Reson Med*. 1990;15:152-157.

42. Marques JP, Kober T, Krueger G, van der Zwaag W, Van de Moortele P-F, Gruetter R. MP2RAGE, a self bias-field corrected

sequence for improved segmentation and T1-mapping at high magnetic field. *Neuroimage*. 2010;49:1271-1281.

43. Haase A, Frahm J, Matthaei D, Hänicke W, Merboldt K-D. FLASH imaging. Rapid NMR imaging using low flip-angle pulses. *J Magn Reson*. 1986;67:258-266.

44. Wansapura JP, Holland SK, Dunn RS, Ball WS. NMR relaxation times in the human brain at 3.0 Tesla. *J Magn Reson Imaging*. 1999;9:531-538.

45. Fernández-Seara MA, Wehrli FW. Postprocessing technique to correct for background gradients in image-based R2* measurements. *Magn Reson Med*. 2000;44:358-366.

46. Peters AM, Brookes MJ, Hoogenraad FG, et al. T2* measurements in human brain at 1.5, 3 and 7 T. *Magn Reson Imaging*. 2007;25:748-753.

47. Noll DC, Nishimura DG, Macovski A. Homodyne detection in magnetic resonance imaging. *IEEE Trans Med Imag*. 1991;10:154-163.

48. Haacke EM, Lindskogj ED, Lin W. A fast, iterative, partial-Fourier technique capable of local phase recovery. *J Magn Reson*. 1991;92:126-145.

49. McGibney G, Smith MR, Nichols ST, Crawley A. Quantitative evaluation of several partial Fourier reconstruction algorithms used in MRI. *Magn Reson Med*. 1993;30:51-59.

50. Zahneisen B, Aksoy M, Maclaren J, Wuerslin C, Bammer R. Extended hybrid-space SENSE for EPI: off-resonance and eddy current corrected joint interleaved blip-up/down reconstruction. *Neuroimage*. 2017;153:97-108.

51. Huber L, Guidi M, Goense J, et al. The magnitude point spread function is an inadequate measure for T2*-blurring in EPI. In: Proceedings of the 23rd Annual Meeting of ISMRM, Toronto, Ontario, Canada, 2015. p 2056.

52. Jesmanowicz A, Bandettini PA, Hyde JS. Single-shot half *k*-space high-resolution gradient-recalled EPI for fMRI at 3 Tesla. *Magn Reson Med*. 1998;40:754-762.

53. Hyde JS, Biswal BB, Jesmanowicz A. High-resolution fMRI using multislice partial *k*-space GR-EPI with cubic voxels. *Magn Reson Med*. 2001;46:114-125.

54. Hagberg GE, Bianciardi M, Brainovich V, Cassara AM, Maraviglia B. Phase stability in fMRI time series: effect of noise regression, off-resonance correction and spatial filtering techniques. *Neuroimage*. 2012;59:3748-3761.

55. Zahneisen B, Assländer J, LeVan P, et al. Quantification and correction of respiration induced dynamic field map changes in fMRI using 3D single shot techniques. *Magn Reson Med*. 2014;71:1093-1102.

56. Maclaren J, Herbst M, Speck O, Zaitsev M. Prospective motion correction in brain imaging: a review. *Magn Reson Med*. 2013;69:621-636.

57. Wilm BJ, Barmet C, Pavan M, Pruessmann KP. Higher order reconstruction for MRI in the presence of spatiotemporal field perturbations. *Magn Reson Med*. 2011;65:1690-1701.

58. Deichmann R, Josephs O, Hutton C, Corfield DR, Turner R. Compensation of susceptibility-induced BOLD sensitivity losses in echo-planar fMRI imaging. *Neuroimage*. 2002;15:120-135.

59. Chen N-K, Oshio K, Panych LP. Improved image reconstruction for partial Fourier gradient-echo echo-planar imaging (EPI). *Magn Reson Med*. 2008;59:916-924.

60. Eichner C, Cauley SF, Cohen-Adad J, et al. Real diffusion-weighted MRI enabling true signal averaging and increased diffusion contrast. *Neuroimage*. 2015;122:373-384.

61. Hernando D, Vigen KK, Shimakawa A, Reeder SB. R2* mapping in the presence of macroscopic B0 field variations. *Magn Reson Med*. 2012;68:830-840.

62. Balla DZ, Sanchez-Panchuelo RM, Wharton SJ, et al. Functional quantitative susceptibility mapping (fQSM). *Neuroimage*. 2014;100:112-124.

63. Langkammer C, Bredies K, Poser BA, et al. Fast quantitative susceptibility mapping using 3D EPI and total variation. *Neuroimage*. 2015;111:622-630.

64. Eichner C, Paquette M, Mildner T, et al. Increased sensitivity and signal-to-noise ratio in diffusion-weighted MRI using multi-echo acquisitions. *Neuroimage*. 2020;221:117172.

65. Ma J, Wehrli FW. Method for image-based measurement of reversible and irreversible contribution to the transverse-relaxation rate. *J Magn Reson B*. 1996;111:61-69.

SUPPORTING INFORMATION

Additional Supporting Information may be found online in the Supporting Information section.

FIGURE S1 Intensity profiles in the phase-encode (PE) direction measured along the broken yellow lines at the positions of the 2.25-mm-diameter rods in the resolution phantom with full-Fourier gradient-echo (fGRE) EPI (A), partial gradient-echo (pGRE) EPI (B), and double-shot EPI with center-out trajectories and intrinsic navigation (DEPICTING) (C). The profiles were obtained from the acquisitions shown in Figure 6 (images are identical to Figure 6K-M). Shaded gray regions indicate the approximate position and size of the rods. Red solid lines show multifrequency reconstruction (MFR)-based distortion corrections (compare with Figure 6E-G), whereas black broken and solid lines correspond to deconvolution-based distortion corrections (DecoDisCo) of frequency offsets without (compare with Figure 6H-J) and with (compare with Figure 6K-M) additional consideration of T_2^* effects, respectively. A decreased width of the region of signal drop at the position of the rods is visible in the DEPICTING image after DecoDisCo with consideration of both $\Delta\nu_0$ and T_2^* effects in comparison with the other correction schemes (blue arrows)

Data S1. Mathematical Symbols

APPENDIX A

POINT-SPREAD FUNCTION OF SPIN-ECHO EPI

A suitable k-space weighting function for (symmetric) SE-EPI is given by

$$H_{SE, n}^{\pm}(t) = e^{-\frac{t^{\pm}+(TE/2)}{T_{2, n}}} \cdot e^{-\frac{|t^{\pm}-(TE/2)|}{T'_{2, n}}} \cdot e^{i 2\pi \Delta \nu_{0, n} t^{\pm}} \cdot \mathbf{1}_{[k_{y, min}, k_{y, max}]}(k_y),$$

(A.1)

where the sampling time $t^{\pm}$ is defined as in Equation 2, and $T_{2,n}$ and $T'_{2,n}$ are the irreversible and the reversible transverse relaxation times, respectively. Following Ma and Wehrli,[65] the two sides of the SE envelope are conveniently characterized by a "rephasing" rate

$$R_{2, n}^{\#} = \frac{1}{T_{2, n}^{\#}} = \frac{1}{T_{2, n}} - \frac{1}{T'_{2, n}}$$

(A.2)

and a "dephasing" rate

$$R_{2, n}^{*} = \frac{1}{T_{2, n}^{*}} = \frac{1}{T_{2, n}} + \frac{1}{T'_{2, n}}.$$

(A.3)

With the same procedures as outlined for GE-EPI, this leads to

$$PSF_{SE, n}^{\pm}(y) = \varepsilon \mathcal{F}^{-1}\left\{H_{SE, n}^{\pm}(k_y)\right\} = \frac{1}{\Delta y} \cdot \left[\frac{e^{q_n^{\#\pm}(2f_p - 1)} - 1}{2q_n^{\#\pm}} + \frac{1 - e^{-q_n^{*\pm}}}{2q_n^{*\pm}}\right],$$

(A.4)

where we have defined a second dimensionless spatial coordinate

$$q_n^{\#\pm}(y) = \frac{N_y \cdot \Delta t_e}{2T_{2, n}^{\#}} - i\pi \left(\Delta \nu_{0, n} \cdot N_y \cdot \Delta t_e \pm \frac{y}{\Delta y}\right).$$

(A.5)

in addition to Equation 4. For a full-Fourier acquisition, the result simplifies to

$$PSF_{fSE, n}^{\pm}(y) = \frac{1}{\Delta y} \cdot \left(\frac{e^{q_n^{\#\pm}} - 1}{2q_n^{\#\pm}} + \frac{1 - e^{-q_n^{*\pm}}}{2q_n^{*\pm}}\right).$$

(A.6)

Note that for $T'_{2,n} \to \infty$ (ie, $T_{2, n} = T_{2, n}^{*}$ and $q_n^{\#\pm} = q_n^{*\pm}$), $PSF_{SE, n}^{\pm}(y) = PSF_{GE, n}^{\pm}(y)$.